Proceedings of the ASME 2020 International Design Engineering Technical Conferences and Computers and Information in Engineering Conference
IDETC/CIE 2020
August 16-19, 2020, St. Louis, MO, USA

IDETC2020-22662

3D BUILD MELT POOL PREDICTIVE MODELING FOR POWDER BED FUSION ADDITIVE MANUFACTURING

Zhuo Yang[1,2], Yan Lu *[2], Ho Yeung[2], and Sundar Kirishnamurty[1]

[1]University of Massachusetts, Amherst, MA, USA
[2]National Institute of Standards and Technology (NIST), Gaithersburg, MD, USA

ABSTRACT

Melt pool size is a critical intermediate measure that reflects the outcome of a laser powder bed fusion process setting. Reliable melt pool predictions prior to builds can help users to evaluate potential part defects such as lack of fusion and over melting. This paper develops a layer-wise Neighboring-Effect Modeling (L-NBEM) method to predict melt pool size for 3D builds. The proposed method employs a feedforward neural network model with ten layer-wise and track-wise input variables. An experimental build using a spiral concentrating scan pattern with varying laser power was conducted on the Additive Manufacturing Metrology Testbed at the National Institute of Standards and Technology. Training and validation data were collected from 21 completed layers of the build, with 6,192,495 digital commands and 118,928 in-situ melt pool coaxial images. The L-NBEM model using the neural network approach demonstrates a better performance of average predictive error (12.12%) by leave-one-out cross-validation method, which is lower than the benchmark NBEM model (15.23%), and the traditional power-velocity model (19.41%).

Keywords: Melt pool size, powder bed fusion, additive manufacturing, machine learning, layer-wise, track-wise

1 INTRODUCTION

Laser powder bed fusion (LPBF) additive manufacturing (AM) uses a laser to melt and fuse spread powder on a build plate. An LPBF machine can precisely scan thin layers of powder to form a designed geometry. The laser delivers thermal energy to the powder to create melt pools once it reaches the melting temperature. Under ideal conditions, the laser should remelt the nearby solidified part to bond the newly melted part [1]. This process occurs both horizontally (track-wise) and vertically (layer-wise) [2, 3].

Melt pool size is a generalized term that represents a group of values such as depth, width, and length. These measurements closely correlate to the part quality [4]. Melt pool width, for example, working closely with hatch distance, can predict void type defects between two adjacent tracks. Melt pool depth, on the other hand, determines the fusion between layers [5]. Figure 1(a) shows an ideal melting condition where the melted areas are well connected between tracks and layers. However, the un-melted powders would appear when the melt pool size doesn't reach the hatch distance and layer thickness. Figure 1(b) shows a lack-of-fusion defect created by insufficient overlap between two melt pool tracks, which leaves track-wise un-melted powders. Figure 1(c) shows the layer-wise un-melted powder between the current and previous layers caused by an insufficient melt pool depth. Either condition could increase porosity in the final part.

Figure 1 shows the defects due to small melt pool sizes. Nevertheless, oversized melt pools may lead to a different type of defects called over melting [6]. If a laser beam frequently re-melts an area with oversized melt pools, this area can be overheated and develops keyholing [7]. Keyhole is a defect that affects both current and future layers. Keyholing creates voids in the current layer, which can significantly affect the powder spreading of the next layer [8, 9].

Though melt pool size is not a property of AM parts, it is a critical process measurement with salient features associated with part quality. Many process parameters can directly or indirectly affect melt pool size. For example, instant energy density has been proved being a major factor in manipulating melt pool size [10, 11]. Melt pool formation is highly sensitive to energy density-related variables such as laser power, scan speed,

*Electronic address: `yan.lu@nist.gov`; Corresponding author

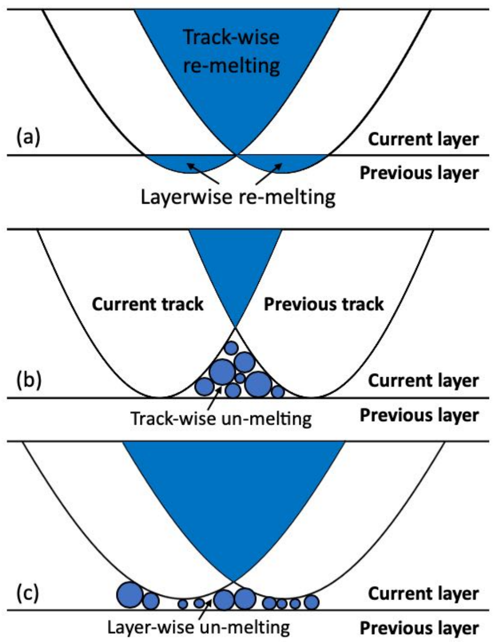

FIGURE 1: The cross-sectional view of two parallel melt pool tracks under three melting conditions. The solid blue area represents the re-melted area. The circles are the un-melted powder particles.

and hatch distance [12]. Energy density determines the maximum thermal input to the powder. Material properties such as heat absorption efficiency determine the actual thermal energy received by the powder [13]. Scan pattern, defining how a laser beam travels, is another important element that affects melt pool size. Experimental studies indicate that part built with the same process parameters but different scan patterns can have distinct thermal fields [14, 15].

If the melt pool size can be predicted before a part is built, users can modify the part design and process setting timely. Physics-based simulation approaches such as finite element analysis (FEA) and computational fluid dynamics (CFD) methods are mature and popular in AM research to predict melt pool size. Pioneer modeling works also reveal that melt pool formation is sensitive to both process parameters and scan patterns [14, 16]. An advantage of the FEA and CFD modeling methods is that they can simulate the effects of any physical parameter [17, 18], for example, various scan patterns. However, the high computational cost is hindering the use of physics-based modeling approaches. A single layer FEA simulation at millimeter-scale may take hours to calculate the interactions between multiple scan tracks. CFD models may be more expensive. This issue becomes noticeable when solving large scale AM problems. The computational cost also prevents the use of these simulations in model-based optimization, because it requires iterative runs to approach the optimal solution.

The data-driven modeling approach becomes a substitute for the physics-based modeling methods to achieve fast predictions. In general, data-driven modeling methods create black-box surrogate models based on experimental data. The computational time may vary from method to method but generally faster than complex simulations [19]. The prediction from surrogate model can usually be made within seconds [11, 20]. However, for data-driven methods, it could be very challenging to characterize process settings and formulate them into a model. For example, scan pattern involves long time series, numerous moving vectors, and dynamic laser spot locations. It is challenging to represent these features using a few variables. And from the perspective of data availability, most AM machines don't export the exact scan path of a build to the users [21].

The authors' previous works developed a data-driven method called Neighboring-Effect Modeling (NBEM) method which was able to address the challenge and predict the melt pool size for a single-layer [14]. However, there were multiple obstacles to further improvement of the model accuracy by extending the single layer to the multi-layers approach. First, it requires multi-layers in-situ melt pool monitoring data, which was not available. Besides, the NBEM factors that designed to capture the features of the single-layer scan strategy cannot quantify the variation between layers.

This study aims to address the research obstacles by developing a novel Layer-wise NBEM (L-NBEM) approach. The L-NBEM method introduces five additional input variables to predict melt pool size using the scan and exposure setting data from the previous layer. An experiment was conducted to collect build commands and melt pool images for multiple layers of one part. This data was used for model construction and validation. The following section mainly introduces the L-NBEM approach, including the physical hypothesis, the modeling variables, and the machine learning method for model training. Section 3 lists the details about the experiment and data. Section 4 presents the results of the L-NBEM model compared to other models. Section 5 discusses the result and future research plan.

2 LAYER-WISE NEIGHBORING-EFFECT MODELING METHOD

This section introduces the background, hypothesis, and modeling variables and method for the L-NBEM approach. The original NBEM method focuses on predicting the melt pool size for a single layer from the process parameters and scan pattern. The fundamental idea is to characterize the neighboring area process settings into two simplified NBEM variables. The proposed L-NBEM method builds on the previous method by introducing more variables to characterize the layer-wise features of process settings for multi-layers AM build.

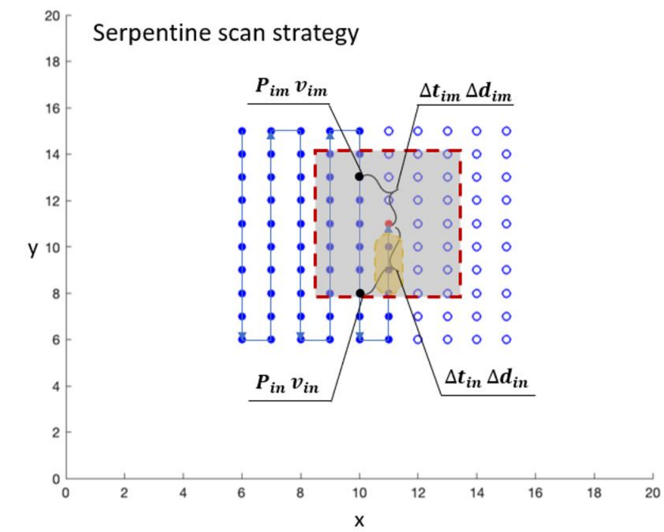

FIGURE 2: Neighboring points in serpentine scan strategy. [14]

2.1 Neighboring-Effect Modeling Method

The fundamental idea of the NBEM method is to use a minimum number of variables to characterize complex scan patterns and the corresponding process parameters. It assumes the melt pool at current laser spot is affected by the nearby region with a neighboring effect, which is a function of the scan pattern. Different scan patterns would visit the neighboring area of a laser scan spot differently. Thus, the time differences and the spatial differences between the previous spots and the current laser spot can be used to characterize the scan pattern.

Figure 2 shows an example of constructing an Ω matrix [14] to capture all the factors affecting the melt pool size within a neighbor region. The red, solid blue, and unfilled blue points in the figure represent the current, previous, and future scan points, respectively. The arrow marks the scan direction of the serpentine scan strategy. The gray area is the neighboring-effect zone enclosed by the red dashed box. This study investigates the neighboring area as a $0.1mm \times 0.1mm$ square. The solid blue points in the gray area are the neighboring points to be included in the Ω matrix. In this work, the points located on the same straight track of the current focal spot are not included in the matrix (dashed yellow area) to avoid over-estimation. It assumes that the laser power and scan speed at the current scan point can cover the effect from these points since it is generally a single track problem.

Parameters P_{im}, v_{im}, P_{in}, v_{in} are the laser power and scan velocity associate to point m and point n, respectively. Δt_{im} and Δd_{im} are the time and distance difference between former point m and current point i. Similarly, Δt_{in} and Δd_{in} are assigned to point n. In this example, $\Delta t_{im} > \Delta t_{in}$ and $\Delta d_{im} > \Delta d_{in}$. Subscript i denotes the i_{ith} spot, which uses the global indexing. m and n are the local indexing referring to the i_{th} point. Collecting the variables for all neighboring points facilitates the formulation of the Ω_i for the current focal point i. Collecting the variables for all neighboring points except the points located in the yellow area facilitates the formulation of the Ω_i for the current focal point i. The dashed yellow area is considered as a single-track problem which is already covered by the laser power and scan speed of current point.

With Ω_i formulated, melt pool area can be expressed as a function of processing parameters and processing history. The smallest Ω_i is an empty matrix which is assigned to the first focal point on a toolpath since no previous points exist at that moment. Points in inner build areas usually have larger Ω_i than those located on the edge. The NBEM factors can be calculated by:

$$f(\Omega_i) = \begin{bmatrix} P_{i1}/v_{i1} \\ P_{i2}/v_{i2} \\ \vdots \\ P_{ij}/v_{ij} \end{bmatrix}^T \begin{bmatrix} f_{\Delta t}(\Delta t_{i1}) & f_{\Delta d}(\Delta d_{i1}) \\ f_{\Delta t}(\Delta t_{i2}) & f_{\Delta d}(\Delta d_{i2}) \\ \vdots & \\ f_{\Delta t}(\Delta t_{ij}) & f_{\Delta d}(\Delta d_{ij}) \end{bmatrix} \tag{1}$$

$\theta_i^{\Delta t}$ and $\theta_i^{\Delta d}$ represent the integrated factor of $f(\Omega_i)$ on time and distance perspective. $f_{\Delta t}(\Delta t_{ij}$ and $f_{\Delta d}(\Delta d_{ij}$ represent the scaling functions of time-lapse and distance, respectively. In Equation (2) and Equation (3), the input laser power P_{ij} of the neighboring point j provides a fundamental impact. Function $f_{\Delta t}(\Delta t_{ij})$ and $f_{\Delta d}(\Delta d_{ij})$ are used to scale the neighboring-effect from 0 (no impact) to 1 (strongest impact). Points geometrically and/or temporally remote to the current focal point are scaled to have minimal impact. Δt_{ij} or Δd_{ij} can be too large to provide any impact since an irradiated area is limited by its size.

$$\theta_i^{\Delta t} = \sum_{j=1}^{j=n} f_{\Delta t}(\Delta t_{ij} \frac{P_{ij}}{v_{ij}} \tag{2}$$

$$\theta_i^{\Delta d} = \sum_{j=1}^{j=n} f_{\Delta d}(\Delta d_{ij} \frac{P_{ij}}{v_{ij}} \tag{3}$$

The time-neighboring-effect focuses on modeling the preheating conditions of the current focal point, which depends on powder cooling rate. The cooling rate can affect the preheating temperature of melting. The literature indicates the temperature of the focal point decreases quickly at the beginning but the total time for cooling and irradiated area can be varied [22,23]. In this work, the time-neighboring-effect is formulated exponentially:

$$f_t(\Delta t_{ij}) = a_1 e^{a_2 \Delta t_{ij}} \quad (4)$$

where $f_t(0) = 1$ and $f_t(\Delta t_{max}) = 0$. The parameters a_1, a_2 and Δt_{max} is a fixed value which is derived from experiments.

The distance-neighboring-effect aims to formulate the spatial impact such as spattering and denuded powder. Simulation and experimental results indicate the denuded width of an irradiated area is ranged from 0.04 mm to 0.06 mm for high-resolution scanning [24, 25]. The distance-neighboring-effect is formulated as:

$$f_d(\Delta d_{ij}) = b_1 e^{b_2 \Delta d_{ij}} \quad (5)$$

where $f_d(0) = 1$ and $f_d(\Delta d_{max}) = 0$. Optimal coefficient b_1 and b_2 will be determined by experimental data. Δt_{max} and Δd_{max} equal to 20 ms and 0.6 mm in this study. The melt pool area, $\tilde{y}_i$, is a function of laser power at current spot, P_i, current scan speed, v_i, and NBEM time and spatial factors $\theta_i^{\Delta t}$ and $\theta_i^{\Delta d}$.

$$\tilde{y}_i = f(P_i, v_i, \theta_i^{\Delta t}, \theta_i^{\Delta d}) \quad (6)$$

2.2 Hypothesis of L-NBEM

In general, melt pool size depends on the energy absorbed by the powder. Higher energy density imported to the powder can make the metal powder particles melted to liquid and fuse to the nearby area easier [26, 27]. Once the metal liquid contacts the powder outside the laser spot, if there is enough additional energy, it would melt more metal powder thus enlarge the melt pool. According to this phenomenon, melt pool size typically is an outcome of thermal energy input. The following hypothesis is made based on this finding.

This study generated the data using the same testbed at one AM build with virgin metal powder. It assumes the machinery and environmental conditions remain the same during the entire process. The model would ignore the variance of powder particle size, changing of chamber temperature and humidity, and fluctuation of laser power. The L-NBEM method of this study considers them as constant parameters for all layers.

Simulations and experiments indicate that the melt pool size is a product of energy input. Laser power and scan speed are two significant components of energy density [28, 29]. The NBEM method includes these two major variables according to the importance of them relates to the energy input. Given the same energy input, however, the melt pool size can be changed due to different preheating temperatures [30]. Higher initial temperature establishes a preheating condition of the powders thus generate larger melt pool size. As a result, factors that may affect the preheating temperature should be included. The track-wise factors in the same layer are characterized by the NBEM method. L-NBEM mainly introduces additional layer-wise factors. The total energy input and cooling time on the previous layer determine the preheating temperature of the current layer. Generally, it is a heat accumulation and releasing process.

The first layer of the part usually builds on the bare build plate with relatively ideal conditions of surface roughness and uniform chamber temperature. The single-track experiment shows the melt pool under the same process parameters produce fewer uncertainties on the bare plate than coarse powders [29]. However, the powders for later layers are spread on the previous layer unless overhanging occurs. Therefore, the L-NBEM method assumes the melting conditions of the previous layer can affect current melt pool formation. To cover this hypothesis, the L-NBEM method would characterize the features of a specific field on the previous layer. This field locates at the projection area of the current NBEM area. Those features from the layer-wise affect to the melt pool size.

Another hypothesis of L-NBEM method is the current layer can only be impacted by the most recent layer. It assumes the layer-wise melt pool features has already covered the thermal history of all former layers.

2.3 Overview of L-NBEM

The L-NBEM method divides the potential factors of the melt pool size into two groups. The first group includes the track-wise factors on the current layer within the NBEM region, the red dashed area in Figure 3. The second group includes the layer-wise factors on the previous layer within the projection of the NBEM region. Figure 3 shows an example of NBEM and L-NBEM regions on Layer 9 and Layer 8. Both layers using the serpentine scan pattern. Arrow lines show the scan path from the beginning to the end. The red and black arrows represent scanned tracks and future tracks, respectively. The orange square represents the NBEM region. Historical points within the NBEM region would be used to calculate the track-wise factors. The red dot located in the center is the current laser spot. The surface plot of Layer 8 represents the melt pool area map. The colormap ranges from 0 mm^2 to 0.04 mm^2. The orange box is the projection area of NBEM region, which crops the L-NBEM region. Historical points located within the L-NBEM region would be used to calculate the layer-wise variables.

Five NBEM factors are formulated to the track-wise input variables: building time from start point to the laser spot (t_i), laser power (P_i), scan speed (v_i) at the laser spot, NBEM time factor ($\theta_i^{\Delta d}$), and NBEM distance factor ($\theta_i^{\Delta d}$). The layer-wise input variables that represent the effect from the previous layer

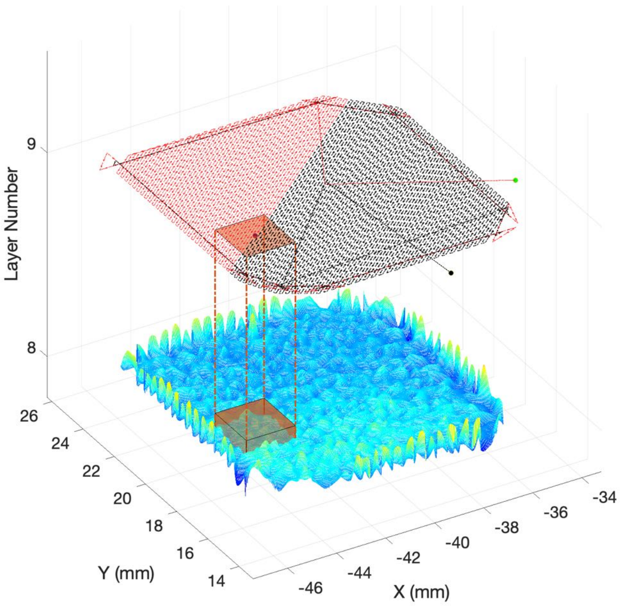

FIGURE 3: An example of two neighboring layers using serpentine scan pattern.

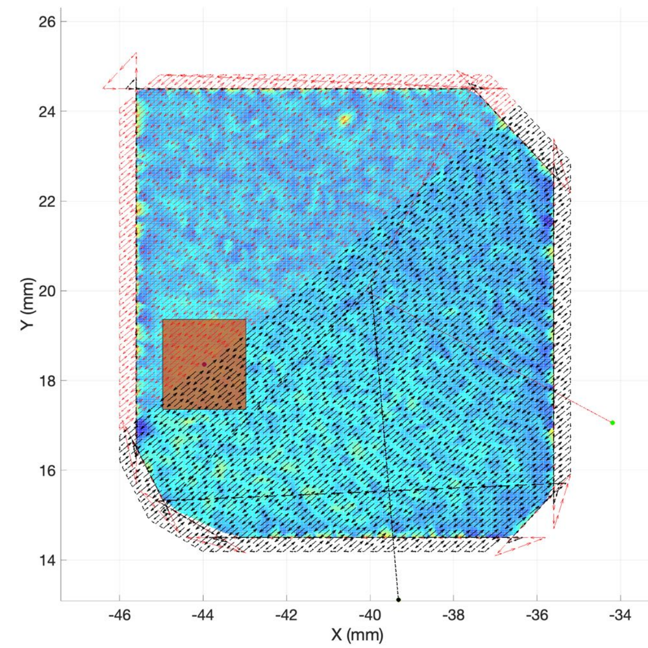

FIGURE 4: 2D view shows the top view of Figure 3 that visualize the layer-wise and track-wise effect when stack two layers together.

are: total energy input on the previous layer (J), laser idle time from the end of the previous layer to start of current layer (λ), mean (A_{avg}), maximum (A_{max}), and standard deviation (A_{var}) of the melt pool area of the L-NBEM region. The general formulation of the L-NBEM model to predict the melt pool area $\tilde{y}_i$ at current laser spot can be presented as:

$$\tilde{y}_i = f(t_i, P_i, v_i, \theta_i^{\Delta t}, \theta_i^{\Delta d}, J, \lambda, A_{avg}, A_{max}, A_{var}) \tag{7}$$

Figure 4 is the 2D view of Figure 3 when stacking the layers into a 2D plot. If the laser spot located on edge, NBEM and L-NBEM would have fewer points. This study uses a square box to filter NBME and L-NBEM fields. However, there is no limitation on the shape of the region.

2.4 Input and Output of L-NBEM

Table 1 lists the input variables in Equation (7) for their unit and function. Variable with star sign indicates it represents the layer-wise effect. Pound sign marks the dependent variable. Energy input is the total energy input from the previous layer, which is a production of laser power at each time step and the total time step. This study sets a constant time step to 10 μs. Thus, the total energy input of any layer could be presented as:

$$J = \sum_{i=1}^{n} P_i \tag{8}$$

Where P_i is the laser power for the i_{th} laser spot, n is the total laser spots for one layer. In fact, the laser spots are not discrete points since they are physically continuously connected. This work uses the time interval (10μs) from the digital commands to separate the laser spots. Thus, the index i of the laser spot is the same to the time step.

Figure 5 shows three examples of melt pool coaxial images. These images were taken at different locations of one layer with same laser power and scan speed. Figure 5(a) is the melt pool less than regular size. Figure 5(b) is the melt pool with average size. Figure 5(c) is the melt pool with very large area. This study chooses area as the output to represent the melt pool size. The grayscale threshold 100 is used to find the contour of the melt pool. The pixels within the contour are considered as the melt pool. The melt pool coaxial image is 120 × 120 pixels, where each pixel is a 8 $\mu m \times 8$ μm square.

Figure 6 shows the melt pool area measured by different threshold values. Figure 6(a) is the original melt pool coaxial image. Figure 6(b) shows the melt pool size by grayscale thresholding set at, 100, 120, and 180. The smallest melt pool area,

TABLE 1: Name, symbol, unit, and function of the variables. The pound sign (#) marks the dependent variables. The star sign (*) marks the variables representing the layer-wise effect.

Variable name	Symbol	Unit	Function
Building time	t_i	ms	Calculate the cumulative heat
Laser power	P_i	W	Input heat source
Scan speed	v_i	mm/s	Affect the energy density at the laser spot
NBEM time #	$\theta_i^{\Delta t}$	N/A	Characterize the time effect
NBEM distance #	$\theta_i^{\Delta d}$	N/A	Characterize the spatial effect
Energy input *, #	J	W	Calculate the total energy input from previous layer
Idle time *	λ	ms	Calculate the cooling time
Mean area *, #	A_{avg}	mm^2	Calculate average melting conditions of previous layer
Maximum area *, #	A_{max}	mm^2	Calculate extreme melting conditions of previous layer
Standard deviation of area *, #	A_{var}	mm^2	Evaluate the variation of melt pool of previous layer

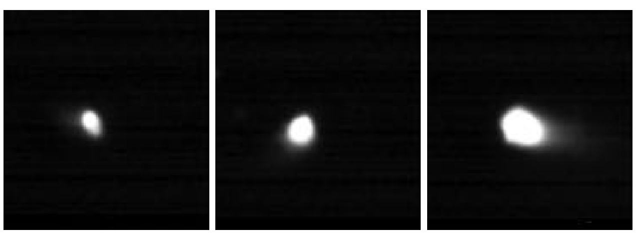

(a) (b) (c)

FIGURE 5: Sample melt pool coaxial images taken at different locations.

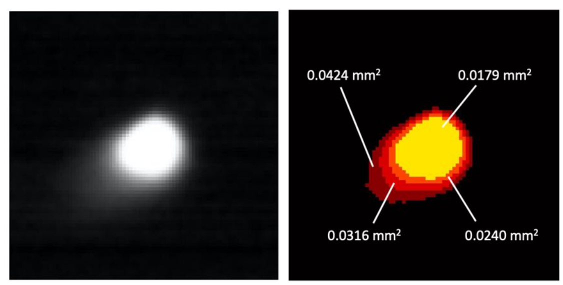

(a) (b)

FIGURE 6: Melt pool area measurement based on different threshold grayscale value.

0.0179 mm^2, is derived based on the highest thresholding 180. The largest melt pool area, 0.0424 mm^2, is measured using the lowest thresholding 80. These two values represent the wrong melt pool size since both thresholding is out of the range found physically. This study selects 100 as the threshold value to measure all the melt pool images. The selected threshold may not be the most accurate number to find the actual melt pool. However, it can represent the melt pool size changes caused by scan pattern and process parameters if all the measurements using the same criteria. Specific to the example shown in Figure 6, the area is 0.0316 mm^2 by grayscale threshold 100.

2.5 Modeling

A feedforward neural network (NN) model is trained to represent the L-NBEM model. Figure 7 plots the structure of the neural network that include input layer, hidden layer, and output layer. The 10 variables in Equation 7 construct the input layer. The hidden layers contain two fully connected layers with 20 nodes for each. Melt pool area constructs the output layer. Levenberg-Marquardt is the activation function. For comparison purpose, polynomial regression is used to build the model by traditional power-speed method.

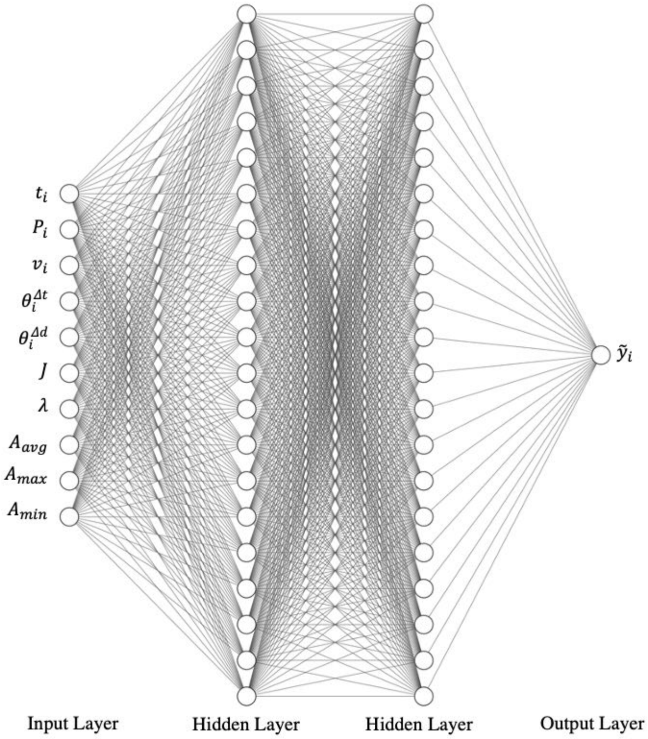

FIGURE 7: Structure of the Neural Network.

2.6 Validation

This study uses the leave-one-out cross-validation (LOOCV) method to validate the proposed method. The data of the layer being validated would not be included in the training dataset for each layer. It would be the validation dataset to validate the model for this layer. An n-layers problem would establish n models for LOOCV.

The criteria for performance evaluation are Average Relative Error Magnitude (AREM) and Average maximum Error Magnitude (Average-MREM) [20]. AREM can represent the average error for all predictions of one particular layer.

$$AREM = \frac{\sum_{i=1}^{m} |y_i - \tilde{y}_i|}{m y_i} \qquad (y_i \neq 0) \tag{9}$$

where m is the total number of validation data points. Parameters y_i and $\tilde{y}_i$ are the actual observation and prediction value of the melt pool area. Since only positive laser power can create melt pool and this experiment always turn on the laser during the build, this study would not have divisor equal to zero.

The average-MREM calculates the average error of the 100 largest error points of each layer. This method aims to evaluate the performance of L-NBEM for extreme conditions. The MREM formula for one layer is:

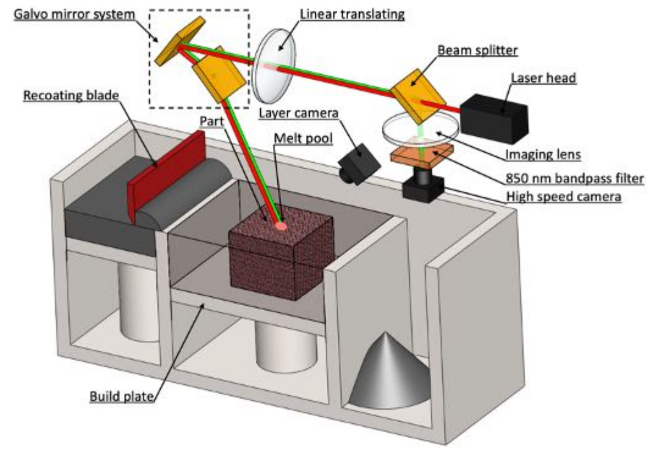

FIGURE 8: The conceptual model of AMMT [14].

$$MREM = max(\frac{|y_i - \tilde{y}_i|}{y_i}) \qquad (y_i \neq 0) \tag{10}$$

3 EXPERIMENT DESIGN

The experiment is conducted on the Additive Manufacturing Metrology Testbed (AMMT) at National Institute of Standards and Technology (NIST) as shown in Figure 8. The AMMT [25] is a fully customized metrology instrument that enables flexible control and measurement of the Laser Powder Bed Fusion process. An in-house developed AM software (SAM), which is capable of stereolithography (STL) slicing, scan path planning, G code generation and interpretation [31], was used to program the different scan strategies for the experiment. Inconel 625 powder and substrate were used, where the substrate has a dimension of 101.6 $mm \times$ 101.6 $mm \times$ 12.7 mm. Twelve rectangular parts (with chambered corners) of dimensions 10 $mm \times$ 10 $mm \times$ 5 mm were laid on the substrate, with a minimum spacing of 10 mm between the parts. Each part was built with a different scan strategy. The melt pool was monitored by a high-speed camera which is optically aligned with the heating laser, such that the image of the melt pool is maintained stationary within the camera's field of view. The camera was triggered at every 200 μs (i.e., 2000 frames per second), with an integration time of 20 μs.

The experiment applies the 'island' spiral concentrating scan strategy to build the part. The part has 250 layers where each layer is 20 μm. To avoid high heat concentration and introduce variance of the island shape, the machine would rotate the centroid angle at each layer. The rotation angle between layers is 83.4 degree and the first layer divide the islands in the vertical intersection as shown in Figure 9(a). After rotating the intersection for 83.4 degrees, the scan pattern for Layer 2 is shown in

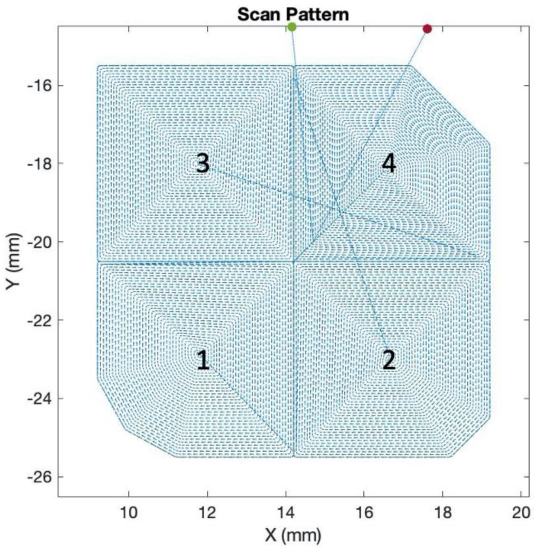

(a)

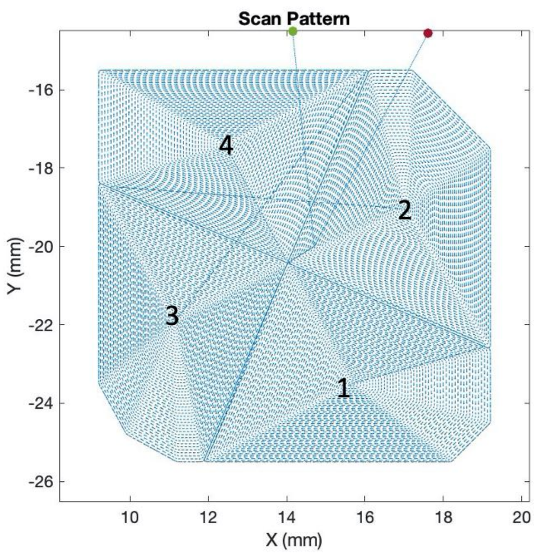

(b)

FIGURE 9: Scan pattern for Layer 1 (a) and Layer 2 (b) of the part. The scan starts at green point and finishes at the red point. Numbers marks the scan order for each island

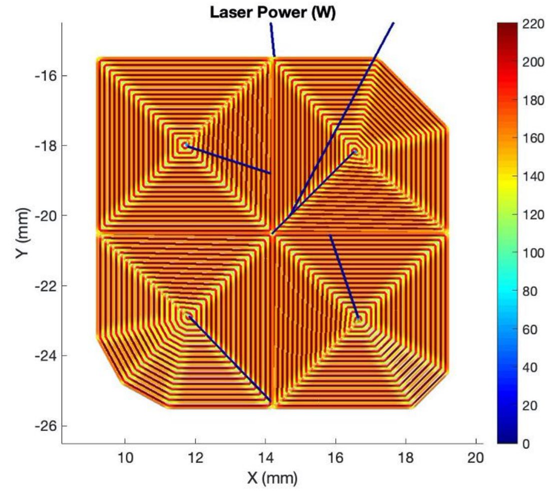

(a)

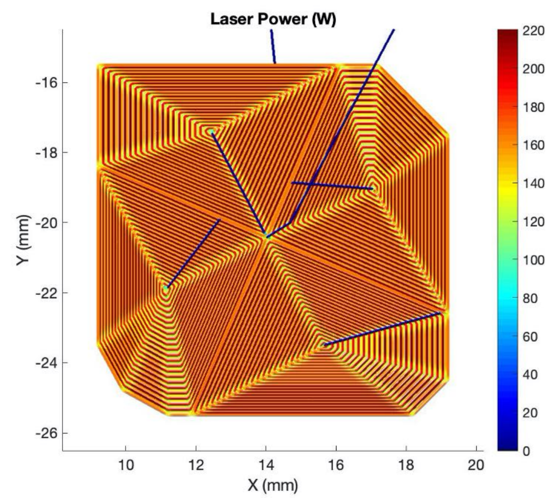

(b)

FIGURE 10: Laser power for Layer 1 and Layer 2

Figure 9(b). For each layer, the laser beam starts at the green point and firstly scan the contour of the part and each island. The laser then moves from the edge spirally concentrating to the center of the first island. After finishing the first island at the island center, it moves to the edge of the second island.

Figure 10 shows the laser power of Layer 1 and Layer 2. The dark blue lines represent when laser traveling between islands with no power input. The machine reduces the scan speed when laser turning direction. The machine reduces the layer power for scan speed to avoid high energy input. The range of laser power and scan speed is from 0W to 234.83 W and 0 to 900 mm/s, respectively.

The AMMT uses XY2-100 control system to control the laser scan [31]. It specifies the laser process parameters (laser coordinates, power, and camera trigger) at each time step. Figure 11 shows the digital commands in a spreadsheet from step 25852 to 25874. Column A and Column B have the laser spot position on the x-axis and y-axis. Column C is the laser power. Column D identifies the coaxial camera trigger. The camera would capture an in-situ image when the value change to 2. The time interval between two steps is 10 μs. The scan speed is calculated from the position between two steps.

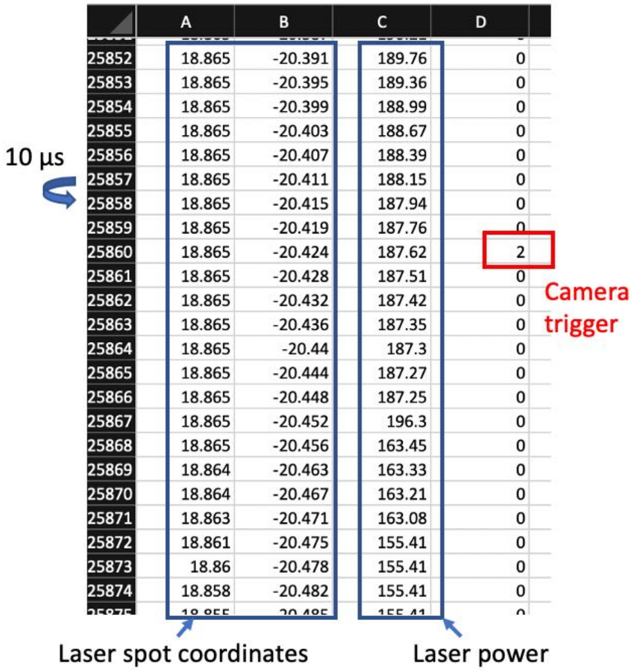

	A	B	C	D
25852	18.865	-20.391	189.76	0
25853	18.865	-20.395	189.36	0
25854	18.865	-20.399	188.99	0
25855	18.865	-20.403	188.67	0
25856	18.865	-20.407	188.39	0
25857	18.865	-20.411	188.15	0
25858	18.865	-20.415	187.94	0
25859	18.865	-20.419	187.76	0
25860	18.865	-20.424	187.62	2
25861	18.865	-20.428	187.51	0
25862	18.865	-20.432	187.42	0
25863	18.865	-20.436	187.35	0
25864	18.865	-20.44	187.3	0
25865	18.865	-20.444	187.27	0
25866	18.865	-20.448	187.25	0
25867	18.865	-20.452	196.3	0
25868	18.865	-20.456	163.45	0
25869	18.864	-20.463	163.33	0
25870	18.864	-20.467	163.21	0
25871	18.863	-20.471	163.08	0
25872	18.861	-20.475	155.41	0
25873	18.86	-20.478	155.41	0
25874	18.858	-20.482	155.41	0

FIGURE 11: The XY2-100 digital commands from step 25852 to step 25874. The column on the left is the time step.

The experiment builds 12 parts at the same time that placed on different positions on the build plate. In other words, the machine needs to scan 12 parts at different locations of each layer. The camera, however, can only focus on one part of each layer. As a result, the experiment collects the melt pool data for the particular part every 12 layers. Finally, a total of 21 layers of data are available for training and validating the L-NBEM model. It include 6,192,495 rows of digital command data for 21 layers and 118,928 melt pool in-situ images. The melt pool area is calculated from these in-situ images using grayscale threshold value 100.

4 RESULT

This section compares the L-NBEM prediction performance with the traditional power-speed model and the NBEM model. For visualization, the melt pool area is mapped into contour plots. All the contour plots, for both measurement and prediction, use the same colormap that ranged from 0 (dark blue) to 0.04 (red) mm^2. Figure 12 shows an example of the transmission from the melt pool images to the melt pool area map. Figure 12(a) distributes all 4,589 melt pool in-situ images of Layer 177 in one map at the position where the image taken. The melt pool area is calculated using a threshold of gray scale 100. Figure 12(b) uses the measured melt pool data to create the contour plot. The melt pool size changes at different locations. For example, the center

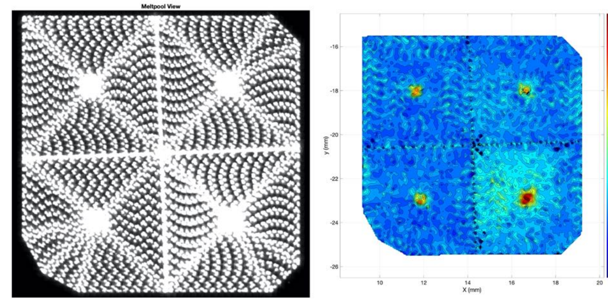

(a) (b)

FIGURE 12: (a) is the map of melt pool in-situ images of Layer 177. (b) is the melt pool area contour plot of this layer.

of each island has larger area than island average. The bottom right island has largest melt pool out of the entire layer.

Figure 13 shows the contour plot from Layer 201 to Layer 249. The solid red box on the left lists the scan pattern and process parameters of Layer 249. The dashed red box on the right lists the scan pattern of Layer 213. Layers present different features on melt pool size, which is mainly caused by the changes in scan strategy. The objective of the L-NBEM model is to predict the variance between layers caused by track-wise and layer-wise variables.

To visualize the result, Figure 14 stacks all the measured layers in one 3D view with a 0.5 transparent ratio. As shown in the figure, the melt pool area average, island average, and oversized melt pool field present significant differences between layers. Some layers have an average area of around 0.02 mm^2. However, others can be as low as 0.015 mm^2. The oversized melt pool is highly clustered at the island center. Furthermore, due to the rotation rule of the island division between layers, the red area twisted from the bottom layer to the top layer. Figure 14 shows the contour plot of the measured melt pool area for all available 21 layers. The colormap is ranged from 0 to 0.04 mm^2.

The melt pool measurement is first compared to the prediction by the traditional power-speed model using the polynomial regression method. The polynomial regression is a form of linear regression in which the relationship between the independent variable x and dependent variable y is modeled as an nth degree polynomial. The power-speed model is popular and reliable in solving most single track problems [29]. The formulation of the model is:

$$\tilde{y}_i = f(P_i, v_i) \tag{11}$$

Figure 15 shows the contour plot of the melt pool predicted from the power-speed model. The AREM and Average-MREM of the LOOCV is 19.41% and 77.30%. As shown in the figure,

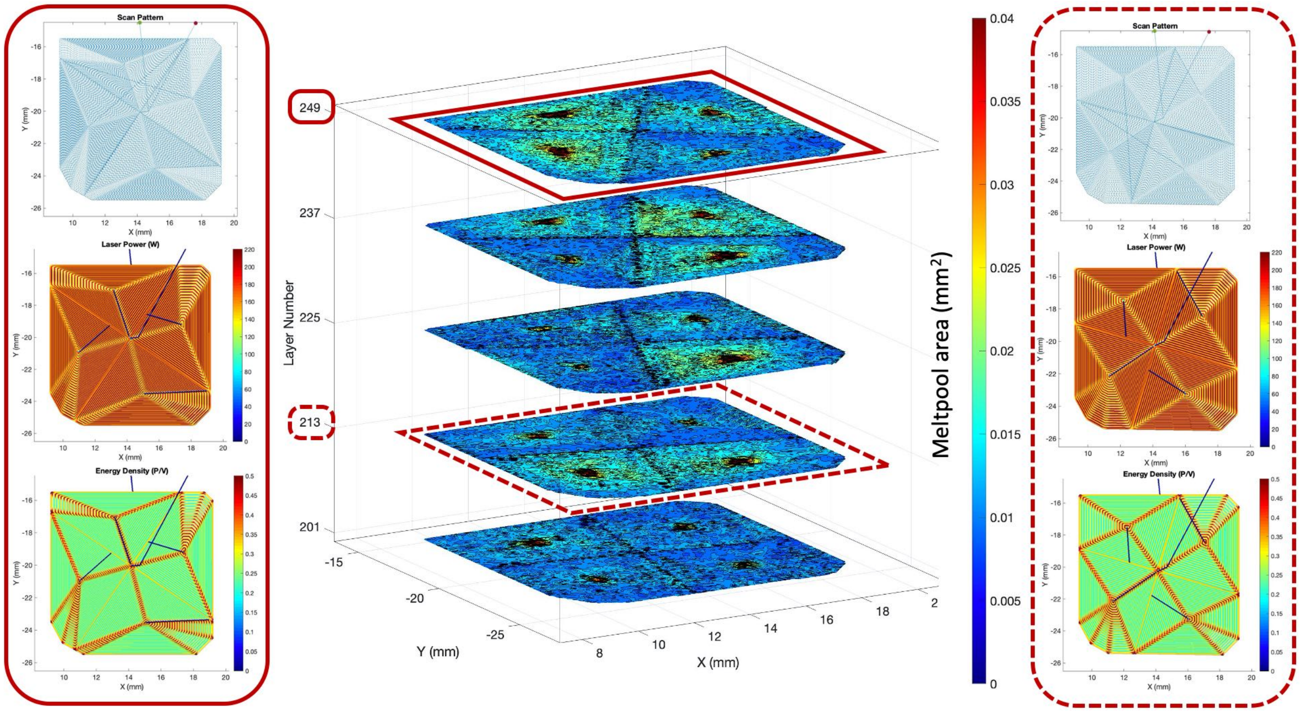

FIGURE 13: The contour plot from Layer 201 to 249. The solid and dashed boxes show the scan pattern for Layer 213 and 249.

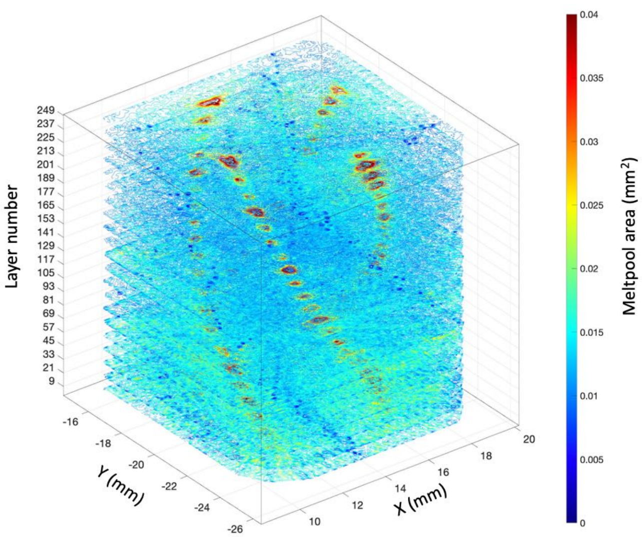

FIGURE 14: The contour plot of the measured melt pool area for all 21 layers.

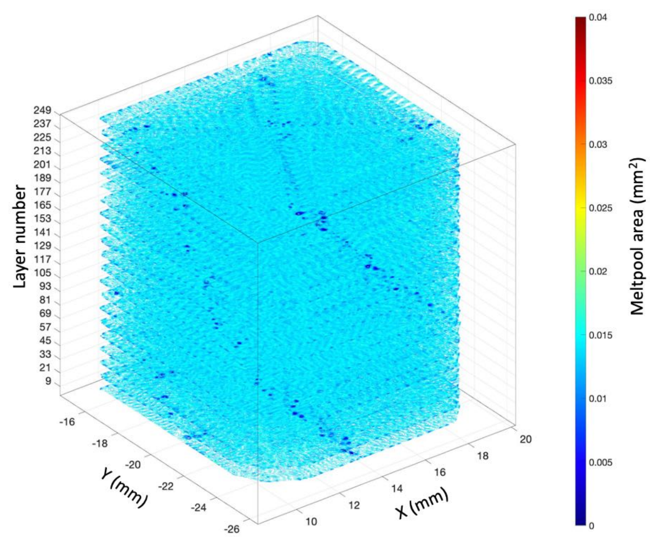

FIGURE 15: The contour plot of the melt pool prediction by power-speed model.

the prediction of each layer is very different to the actual melt pool area. It can predict some fields with relatively small melt pool due to insufficient energy input, the darker blue area. However, the major issue of this model is that it cannot distinguish the difference caused by the scan pattern, such as irregular melt pool field at the island center.

For comparison, the NBEM method is used to single layer model for all 21 layers. It is also the first time to test this approach using multi-layers experimental data. The NBEM model, which was designed for solving single layer problems, can pre-

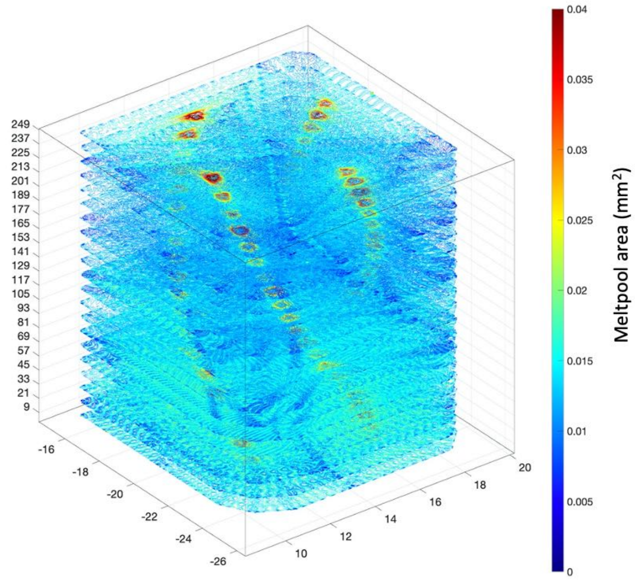

FIGURE 16: The contour plot of the melt pool size prediction by the NBEM model.

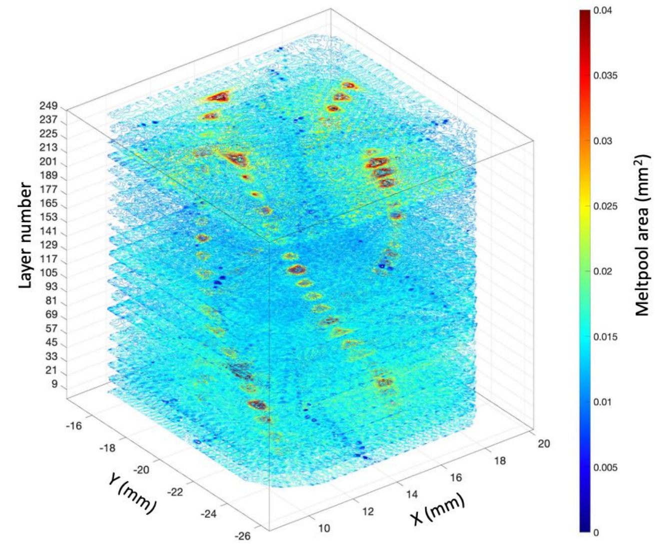

FIGURE 17: The contour plot of the melt pool prediction by the L-NBEM model.

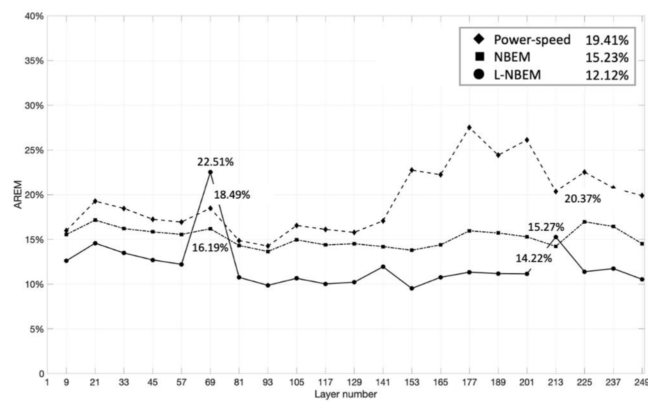

FIGURE 18: LOOCV AREM for all 21 layers of power-speed (P-v), NBEM, and L-NBEM methods.

dict the irregular melt pool area due to scan pattern changes. The NBEM model is trained using the quadratic polynomial regression method. The AREM and Average-MREM of LOOCV is 15.23% and 70.3%, respectively.

Figure 16 shows the melt pool area predicted by the NBEM method. Compared to Figure 14, the model can predict the regular and irregular melt pool located on the layers. The differences between layers are also reflected on the contour plots. However, due to a lack of consideration for the layer-wise effect, predictions for the the details remain an issue.

Figure 17 shows the prediction resulted from the L-NBEM model. The LOOCV result of this method presents the lowest AREM and average-MREM, 12.12% and 64.13%, respectively. The contour plot based on the L-NBEM prediction is the closest to the actual measurement compared to the power-speed and NBEM models.

Figure 18 shows the LOOCV AREM for the melt pool predictions using the power-speed, NBEM, and L-NBEM models based on the data for all the 21 layers. L-NBEM has the lowest global average AREM. L-NBEM also demonstrates the lowest AREM for 19 layers. However, Layer 69 of L-NBEM presents the largest AREM (22.52 %) while the NBEM model presents the lowest AREM (14.22%) for Layer 213.

5 DISCUSSION AND FUTURE WORK

The objective of this work is to extend the NBEM method from a single layer approach to a multi-layer approach for melt pool size prediction. For this purpose, this study introduces five additional variables to enhance the model performance. Generally speaking, the track-wise variables captured in the NBEM model characterize the effect from the scan pattern of the current layer. The newly added layer-wise variables characterize the effect of the previous layers. By introducing these new variables, L-NBEM can predict the melt pool size better for 3D AM builds.

An experiment provides more than 100,000 coaxial melt pool in-situ images and 6 million high sampling digital commands to validate the effectiveness of the proposed approach. All the data are deployed for training and validating the L-NBEM model using the LOOCV method. The L-NBEM model shows the lowest AREM compared to both the traditional power-speed and the NBEM models. The L-NBEM model can predict both regular melt pools that following general energy density rules and irregular melt pools introduced by the scan pattern. The model may be helpful for layerwise feedback process control of LPBF machines.

However, it is also observed that the L-NBEM model cannot guarantee a predictive accuracy for all layers. For example, Layer 69 is an outstanding layer that shows large predictive errors. The AREM of that layer reaches 22.51% which is higher than that of the NBEM model and that of the power-speed model. The error could be introduced because of the neural network construction. Various neural network configurations were tried, such as changing the number of hidden layers and neurons, different functions, and different parameters. However, none of them improved the results significantly. Layers with outstanding prediction errors exist and show up randomly. In the future, a more comprehensive machine learning approach would be investigated to reduce the modeling inconsistency. Model uncertainty quantification should be considered since such modeling uncertainties may significantly affect the melt pool size prediction [32, 33].

The prediction error may also be generated from the experimental method. The part was built with 250 thin layers. However, due to a data acquisition limitation, the in-situ melt pool monitoring data was captured every 12 layers. Because of that, some layer-wise variables were calculated from estimates instead of direct measurements. This could lead to many data errors prior to model training. A more precise experimental design may help address this issue.

Future work would focus on building the correlation between melt pool size and final material properties such as porosity and residual stress. When preparing this paper, the co-authors were working on collecting the ex-situ data of the parts using X-ray computed tomography (XCT) scan. The preliminary findings based on the XCT scan data indicate that the distribution of the voids is similar to the melt pool area distribution. As shown in Figure 19, larger melt pool size regions (measured) usually locate at the center of each island at every layer. Due to the island division rotation strategy, these regions form a circle after projecting all the layers into a 2D figure. Coincidentally, the preliminary result of the XCT data shows the voids of the part in a similar pattern. A physics based explanation is that large melt pool size regions reflect the overheating at the island center during the process. The overheating may create keyholes and finally produce the voids. Future work would investigate the potential correlation between melt pool size and porosity. If part porosity and melt pool size have a great correlation, it would be possible to predict voids using in-situ melt pool images.

6 DISCLAIMER

Certain commercial systems are identified in this paper. Such identification does not imply recommendation or endorsement by NIST; nor does it imply that the products identified are necessarily the best available for the purpose. Further, any opinions, findings, conclusions, or recommendations expressed in this material are those of the authors and do not necessarily reflect the views of NIST or any other supporting U.S. government or corporate organizations.

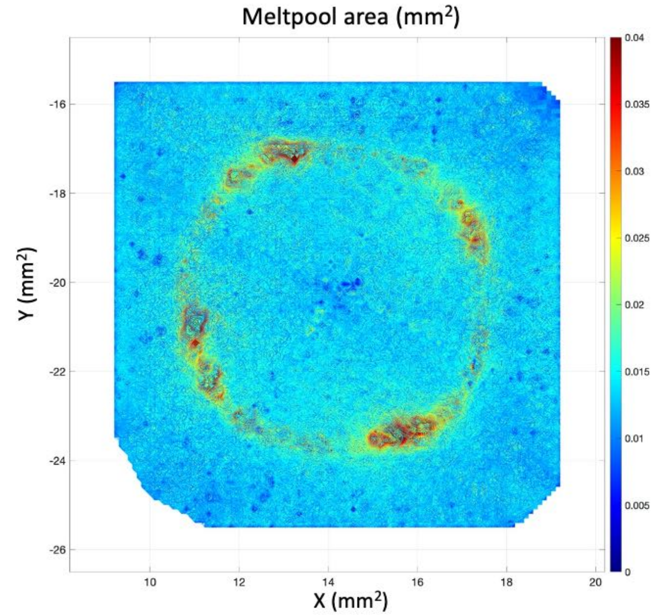

FIGURE 19: 2D top view for the measure melt pool contour plot after stacking all 21 layers together.

ACKNOWLEDGMENT

This material is based upon work supported by the National Institute of Standards and Technology (NIST) under Cooperative Agreement number NIST 70NANB18H258.

REFERENCES

[1] King, W., Anderson, A. T., Ferencz, R. M., Hodge, N. E., Kamath, C., and Khairallah, S. A., 2015. "Overview of modelling and simulation of metal powder bed fusion process at lawrence livermore national laboratory". *Materials Science and Technology,* ***31***(8), pp. 957–968.

[2] Luo, N., Scheitler, C., Ciftci, N., Galgon, F., Fu, Z., Uhlenwinkel, V., Schmidt, M., and Körner, C., 2020. "Preparation of fe-co-b-si-nb bulk metallic glasses by laser powder bed fusion: Microstructure and properties". *Materials Characterization,* ***162***, p. 110206.

[3] Matilainen, V., Piili, H., Salminen, A., Syvänen, T., and Nyrhilä, O., 2014. "Characterization of process efficiency improvement in laser additive manufacturing". *Physics Procedia,* ***56***, pp. 317–326.

[4] Frazier, W. E., 2014. "Metal additive manufacturing: a review". *Journal of Materials Engineering and Performance,* ***23***(6), pp. 1917–1928.

[5] Gong, H., Rafi, K., Gu, H., Starr, T., and Stucker, B., 2014. "Analysis of defect generation in ti–6al–4v parts made using powder bed fusion additive manufacturing processes". *Additive Manufacturing,* ***1***, pp. 87–98.

[6] Fox, J. C., Lopez, F., Lane, B. M., Yeung, H., and Grantham, S., 2016. "On the requirements for model-based thermal control of melt pool geometry in laser powder bed fusion additive manufacturing". In Proceedings of the 2016 Material Science & Technology Conference, Salt Lake City, pp. 133–140.

[7] King, W. E., Barth, H. D., Castillo, V. M., Gallegos, G. F., Gibbs, J. W., Hahn, D. E., Kamath, C., and Rubenchik, A. M., 2014. "Observation of keyhole-mode laser melting in laser powder-bed fusion additive manufacturing". *Journal of Materials Processing Technology,* ***214***(12), pp. 2915–2925.

[8] Matilainen, V.-P., Piili, H., Salminen, A., and Nyrhilä, O., 2015. "Preliminary investigation of keyhole phenomena during single layer fabrication in laser additive manufacturing of stainless steel". *Physics Procedia,* ***78***, pp. 377–387.

[9] Khairallah, S. A., Anderson, A. T., Rubenchik, A., and King, W. E., 2016. "Laser powder-bed fusion additive manufacturing: Physics of complex melt flow and formation mechanisms of pores, spatter, and denudation zones". *Acta Materialia,* ***108***, pp. 36–45.

[10] Lopez, F., Witherell, P., and Lane, B., 2016. "Identifying uncertainty in laser powder bed fusion additive manufacturing models". *Journal of Mechanical Design,* ***138***(11).

[11] Yang, Z., Hagedorn, T., Eddy, D., Krishnamurty, S., Grosse, I., Denno, P., Lu, Y., and Witherell, P., 2017. "A domain-driven approach to metamodeling in additive manufacturing". In ASME 2017 International Design Engineering Technical Conferences and Computers and Information in Engineering Conference, American Society of Mechanical Engineers Digital Collection.

[12] Ciurana, J., Hernandez, L., and Delgado, J., 2013. "Energy density analysis on single tracks formed by selective laser melting with cocrmo powder material". *The International Journal of Advanced Manufacturing Technology,* ***68***(5-8), pp. 1103–1110.

[13] Devesse, W., De Baere, D., and Guillaume, P., 2014. "The isotherm migration method in spherical coordinates with a moving heat source". *International Journal of Heat and Mass Transfer,* ***75***, pp. 726–735.

[14] Yang, Z., Lu, Y., Yeung, H., and Krishnamurty, S., 2020. "From scan strategy to melt pool prediction: A neighboring-effect modeling method". *Journal of Computing and Information Science in Engineering,* ***20***(5).

[15] Gibson, I., Rosen, D. W., Stucker, B., et al., 2014. *Additive manufacturing technologies*, Vol. 17. Springer.

[16] Beal, V., Erasenthiran, P., Hopkinson, N., Dickens, P., and Ahrens, C., 2006. "The effect of scanning strategy on laser fusion of functionally graded h13/cu materials". *The International Journal of Advanced Manufacturing Technology,* ***30***(9-10), pp. 844–852.

[17] Yan, W., Ge, W., Smith, J., Wagner, G., Lin, F., and Liu, W. K., 2015. "Towards high-quality selective beam melting technologies: modeling and experiments of single track formations". In 26th Annual international symposium on solid freeform fabrication, Austin, Texas.

[18] King, W. E., Anderson, A. T., Ferencz, R. M., Hodge, N. E., Kamath, C., Khairallah, S. A., and Rubenchik, A. M., 2015. "Laser powder bed fusion additive manufacturing of metals; physics, computational, and materials challenges". *Applied Physics Reviews,* ***2***(4), p. 041304.

[19] Shao, T., 2007. *Toward a structured approach to simulation-based engineering design under uncertainty*. University of Massachusetts Amherst.

[20] Yang, Z., Eddy, D., Krishnamurty, S., Grosse, I., Denno, P., and Lopez, F., 2016. "Investigating predictive metamodeling for additive manufacturing". In ASME 2016 International Design Engineering Technical Conferences and Computers and Information in Engineering Conference, American Society of Mechanical Engineers Digital Collection.

[21] Yeung, H., Neira, J., Lane, B., Fox, J., and Lopez, F., 2016. "Laser path planning and power control strategies for powder bed fusion systems". In The Solid Freeform Fabrication Symposium, pp. 113–127.

[22] Manvatkar, V., De, A., and DebRoy, T., 2014. "Heat transfer and material flow during laser assisted multi-layer additive manufacturing". *Journal of Applied Physics,* ***116***(12), p. 124905.

[23] Bertoli, U. S., Guss, G., Wu, S., Matthews, M. J., and Schoenung, J. M., 2017. "In-situ characterization of laser-powder interaction and cooling rates through high-speed imaging of powder bed fusion additive manufacturing". *Materials & Design,* ***135***, pp. 385–396.

[24] Hooper, P. A., 2018. "Melt pool temperature and cooling rates in laser powder bed fusion". *Additive Manufacturing,* ***22***, pp. 548–559.

[25] Lane, B., Mekhontsev, S., Grantham, S., Vlasea, M., Whiting, J., Yeung, H., Fox, J., Zarobila, C., Neira, J., McGlauflin, M., et al., 2016. "Design, developments, and results from the nist additive manufacturing metrology testbed (ammt)". In Solid Freeform Fabrication Symposium, Austin, TX, pp. 1145–1160.

[26] Ly, S., Rubenchik, A. M., Khairallah, S. A., Guss, G., and Matthews, M. J., 2017. "Metal vapor micro-jet controls material redistribution in laser powder bed fusion additive manufacturing". *Scientific reports,* ***7***(1), pp. 1–12.

[27] Lane, B., Moylan, S., Whitenton, E. P., and Ma, L., 2016. “Thermographic measurements of the commercial laser powder bed fusion process at nist”. *Rapid prototyping journal*.

[28] Foroozmehr, A., Badrossamay, M., Foroozmehr, E., and Golabi, S., 2016. “Finite element simulation of selective laser melting process considering optical penetration depth of laser in powder bed”. *Materials & Design,* ***89***, pp. 255–263.

[29] Lu, Y., Yang, Z., Eddy, D., and Krishnamurty, S., 2018. “Self-improving additive manufacturing knowledge management”. In ASME 2018 International Design Engineering Technical Conferences and Computers and Information in Engineering Conference, American Society of Mechanical Engineers Digital Collection.

[30] Vasinonta, A., Beuth, J. L., and Griffith, M., 2007. “Process maps for predicting residual stress and melt pool size in the laser-based fabrication of thin-walled structures”.

[31] Yeung, H., Lane, B. M., Donmez, M., Fox, J. C., and Neira, J., 2018. “Implementation of advanced laser control strategies for powder bed fusion systems”. *Procedia Manufacturing,* ***26***, pp. 871–879.

[32] Moges, T., Ameta, G., and Witherell, P., 2019. “A review of model inaccuracy and parameter uncertainty in laser powder bed fusion models and simulations”. *Journal of manufacturing science and engineering,* ***141***(4).

[33] Moges, T., Yan, W., Lin, S., Ameta, G., Fox, J., and Witherell, P., 2018. “Quantifying uncertainty in laser powder bed fusion additive manufacturing models and simulations”. In Solid Freeform Fabrication Symposium An Additive Manufacturing Conference.